On numerical aspects of simulating flow past a circular cylinder

HONGYI JIANG[1†], LIANG CHENG[1,2], AND HONGWEI AN[1]

[1]School of Civil, Environmental and Mining Engineering, The University of Western Australia, 35 Stirling Highway, Crawley, WA 6009, Australia

[2]State Key Laboratory of Coastal and Offshore Engineering, Dalian University of Technology, Dalian, 116024, China

Abstract

Three-dimensional (3D) direct numerical simulation (DNS) results of flow past a circular cylinder are influenced by numerical aspects, e.g. the spanwise domain length and the lateral boundary condition adopted for the simulation. It is found that inappropriate numerical setup which restricts the development of intrinsic wake structure leads to an over-prediction of the onset point of the secondary wake instability (Re_{cr}). A best practice of the numerical setup is presented for the accurate prediction of Re_{cr} by DNS while minimizing the computational cost. The cylinder span length should be chosen based on the intrinsic wavelength of the wake structure to be simulated, whereas a long span length is not necessary. For the wake transitions above Re_{cr}, since the wake structures no longer follow particular wavelengths but become disordered and chaotic, a span length of more than 10 cylinder diameters (approximately three times the intrinsic wavelength) is recommended for the simulations to obtain wake structures and hydrodynamic forces that are not strongly restricted by the numerical setup. The performances of the periodic and symmetry lateral boundary conditions are compared and discussed. The symmetry boundary condition is recommended for predicting Re_{cr}, while the periodic boundary condition is recommended for simulating the wake structures above Re_{cr}. The general conclusions drawn through a circular cylinder are expected to be applicable to other bluff body configurations.

[†]Email address for correspondence: hongyijiang88@gmail.com

Key words: Direct numerical simulation; Circular cylinder; Wake transition; Spanwise domain length; Boundary condition

1. Introduction

Steady incoming flow past a long bluff body or a set of bluff bodies at relatively low Reynolds numbers (*Re*) has been studied extensively with numerical approaches such as direct numerical simulation (DNS) and large eddy simulation (LES). As a classical case, flow past a circular cylinder is governed by a single dimensionless parameter *Re* (= *UD*/*v*), defined based on the approaching flow velocity *U*, the cylinder diameter *D* and the kinematic viscosity of the fluid *v*. For bluff bodies with different cross-sectional shapes or multiple bluff bodies, the geometric configuration of the bodies also influences the flow. For simplicity, the present study focuses on flow past a circular cylinder. The general conclusions drawn through a circular cylinder, however, are expected to be applicable to other bluff body configurations.

The major focuses of previous studies on flow past a circular cylinder at relatively low *Re* values were on wake transition to three-dimensional (3D) instabilities and corresponding wake structures in different flow regimes. It is well-known that the flow undergoes a transition to the secondary wake instability when *Re* reaches to a moderate threshold of $Re_{cr} \sim 190$ (e.g. Williamson, 1996; Barkley and Henderson, 1996). The first 3D instability mode is represented by an ordered Mode A vortex structure (before the natural evolvement of vortex dislocations) which has a spanwise wavelength λ_A of 3.96 at Re_{cr} and reduces slightly with increase of *Re* (Williamson, 1996; Barkley and Henderson, 1996). For *Re* ranging from 230 to 250, the wake transitions gradually to Mode B, with a spanwise wavelength λ_B of ~ 0.82 (Williamson, 1996). In order to resolve the 3D flow structures for $Re > Re_{cr}$, the numerical simulation is extended to 3D, which requires the selection of appropriate spanwise domain length L_z and boundary conditions at the two lateral boundaries perpendicular to the cylinder span. For simplicity, L_z, λ_A and λ_B in this paper are all normalized with the cylinder diameter.

It is important to note that λ_A and λ_B denote the most unstable spanwise wavelengths of Mode A and Mode B, respectively. They are intrinsic properties of the flow and are usually obtained from experiments or linear stability analysis. However, in typical 3D DNS, if L_z is not specified as an integer multiple of the most unstable spanwise wavelength, the simulated wavelength may be dependent on the choice of L_z. In order to distinguish it from the most unstable wavelength, the simulated wavelength will be denoted as λ (which is also normalized with the cylinder diameter).

The influence of L_z on the convergence of 3D numerical results of flow past a circular cylinder has been studied extensively in the literature. The 3D DNS study based on a spectral element method (SEM) by Gioria et al. (2011) with Re = 400 and L_z = 0 – 12 observed the emergence of flow three-dimensionality at $L_z \sim 0.35$ and a converged 3D flow for $L_z \geq 6$. Based on a finite difference method (FDM) approach, Lei et al. (2001) performed 3D DNS at Re = 1000 with L_z ranging from 0 to 6, and found that the force coefficients and pressure around the cylinder generally converged at $L_z \geq 2$. Labbé and Wilson (2007) performed LES with Re = 40 – 1000 and $L_z = 0.5\pi$, π, and 2π, and observed increased numbers of Mode A vortex pairs at Re of 200 and 225 with increase of L_z. They also suggested a minimum L_z of 4 for $Re \leq 300$ and a minimum L_z of between 0.5π and 1.0π for higher Re values in order to accurately predict the force coefficients and 3D wake structures. Karniadakis and Triantafyllou (1992) performed 3D DNS based on a SEM approach at Re = 225 and 300, and observed similar power spectra and flow patterns for L_z of π and 2π. The DNS based on SEM by Posdziech and Grundmann (2001) found that the Strouhal number and base pressure coefficient at Re = 280 converged and matched independent experimental results at $L_z = 2\lambda_A$ (= 6.74).

The influence of L_z on the development of vortex dislocation has also been studied in the literature. Extensive experimental studies have shown that the ordered Mode A vortex structure will evolve spontaneously into a more stable pattern with large-scale vortex dislocations (e.g. Williamson, 1992, 1996). This phenomenon has also been confirmed through numerical studies based on different mathematical

formulations (e.g. Henderson, 1997; Braza et al., 2001; Behara and Mittal, 2010). In a SEM based DNS study by Henderson (1997), time-periodic Mode A was observed at *Re* of 190 and 195 when L_z was restricted to 3.96 (~ λ_A), whereas spatiotemporal chaotic wake structures were observed at *Re* of 220 when L_z was extended to 14.78 (~ $4\lambda_A$). Similarly, at *Re* = 265, time-periodic Mode B was observed when L_z = 0.822 (~ λ_B), whereas a chaotic mixture of Modes A and B was observed when L_z = 13.152 (~ $16\lambda_B$). In a finite volume method (FVM) based DNS study by Persillon and Braza (1998), vortex dislocation was not observed due to the use of a small L_z of 2.25. In a follow-up study by Braza et al. (2001), a much larger L_z of 12 was used, and large-scale vortex dislocations were observed at *Re* = 220. Based on a finite element method (FEM) approach, the DNS by Behara and Mittal (2010) also observed vortex dislocations at *Re* of 200 and 220 with a relatively large L_z of 10. In general, the above studies showed that vortex dislocations can be observed under relatively large L_z but are suppressed by short L_z of about the wavelength of the wake structure. However, the shortest L_z that can be adopted for relatively L_z-independent simulations involving vortex dislocations has not been addressed.

On the other hand, less attention has been paid to the influence of the choice of the lateral boundary conditions (BCs) on the prediction of the flow characteristics including the Re_{cr}, spanwise wavelength, and wake structure. In fact, the prediction of flow characteristics is dependent on both the L_z value and the lateral BC.

Two kinds of BCs are usually adopted at the lateral boundaries to approximate an infinite span length in numerical studies, i.e. the periodic lateral BC (adopted by, e.g., Karniadakis and Triantafyllou, 1992; Henderson, 1997; Braza et al., 2001; Lei et al., 2001; Posdziech and Grundmann, 2001; Zhao et al., 2013) and the symmetry lateral BC (adopted by, e.g., Labbé and Wilson, 2007; Behara and Mittal, 2010; Tong et al., 2014). The periodic BC imposes a spanwise periodicity of L_z on the flow through the linkage between the two lateral boundaries:

$$u_i(x, y, z = 0, t) = u_i(x, y, z = L_z, t) \tag{1.1}$$

$$\partial u_i/\partial z(x, y, z = 0, t) = \partial u_i/\partial z(x, y, z = L_z, t) \tag{1.2}$$

$$p(x, y, z = 0, t) = p(x, y, z = L_z, t) \tag{1.3}$$

$$\partial p/\partial z(x, y, z = 0, t) = \partial p/\partial z(x, y, z = L_z, t) \quad (1.4)$$

where (x, y, z) are Cartesian coordinates (see Fig. 1), u_i is the velocity component in the direction x_i (= $(x_1, x_2, x_3) = (x, y, z)$), t is time and p is pressure. On the other hand, the symmetry BC treats both of the lateral boundaries as symmetry planes:

$$\partial u_x/\partial z = \partial u_y/\partial z = \partial p/\partial z = u_z = 0 \qquad \text{at } z = 0 \text{ and } z = L_z \quad (1.5)$$

Previous studies showed that either of the two BCs can be used to reproduce the ordered Mode A and Mode B vortex structures, due to the spanwise periodicity of the two modes (Williamson, 1996). When the periodic BC is imposed at the lateral boundaries, the simulated flow is forced to contain only an integer number (denoted as n) of the vortex pairs in the spanwise direction to satisfy the BC at the lateral boundaries. In contrast, when the symmetry BC is employed at the lateral boundaries, the number of vortex pairs in the simulated flow is constrained to $0.5n$, as all the planes in the middle of the adjacent positive and negative vortices are symmetrical. The symmetry BC allows a half of a vortex pair to be captured. Consequently, the simulated spanwise wavelength λ is restricted to L_z/n for the periodic BC and $2L_z/n$ for the symmetry BC, and thus may be different from the most unstable wavelength (λ_A or λ_B) of the flow. Therefore, the accuracy of the simulation may be dependent on the choices of not only the L_z value but also the lateral BC. It is also noted that the symmetry BC condition characterized by Eq. (1.5) may also rule out the possibility of travelling waves such as oblique vortex shedding, which warrants a further investigation.

(a)

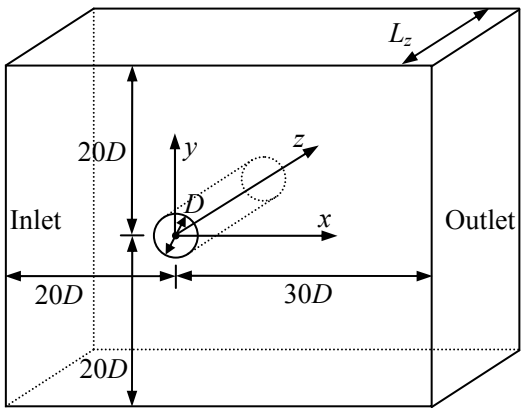

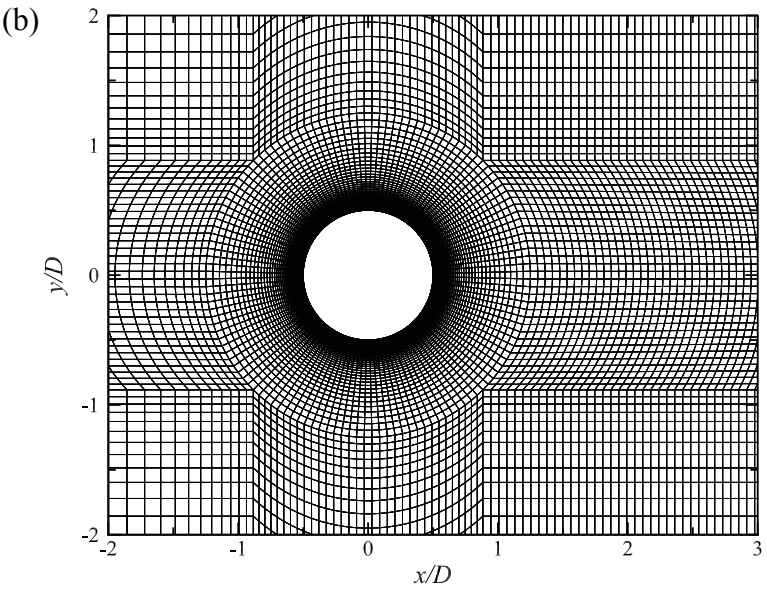

Fig. 1. (a) Schematic model of the computational domain, and (b) Close-up view of the mesh in the *x*-*y* plane near the cylinder.

To complement the earlier works, the primary aim of this study is to investigate the combined influence of the lateral BC and L_z on the prediction of Re_{cr} as well as the Mode A and Mode B flows at $Re_{cr} < Re < 300$, for which a general guideline on the choices of the lateral BC and L_z for DNS has not been proposed in the literature (although DNS has been used extensively for predicting bluff body flows).

For other bluff body configurations, e.g. a square cylinder (Robichaux et al., 1999), an elliptic cylinder (Leontini et al., 2015), a circular ring (Sheard et al., 2003), two circular cylinders in staggered arrangements (Carmo et al., 2008), a rotating cylinder near a moving wall (Rao et al., 2015), etc., similar Mode A and Mode B flows (as well as other modes) with similar spanwise wavelengths were obtained based on stability analysis. In addition to bluff body flows, stability analysis of the flow over a backward-facing step (Barkley et al., 2002) and the flow through a partially blocked channel (Griffith et al., 2007) also found that the onset of the secondary instability was represented by a 3D mode with a specific spanwise wavelength. Hence the general conclusions drawn from the present study through a circular cylinder are expected to provide guidance on the choices of the lateral BC and L_z for a non-linear DNS analysis of the above flows.

2. Numerical model

2.1. Numerical method

The DNS have been carried out with OpenFOAM (www.openfoam.org) through solution of the continuity and incompressible Navier-Stokes equations:

$$\frac{\partial u_i}{\partial x_i} = 0 \tag{2.1}$$

$$\frac{\partial u_i}{\partial t} + u_j \frac{\partial u_i}{\partial x_j} = -\frac{1}{\rho}\frac{\partial p}{\partial x_i} + \nu \frac{\partial^2 u_i}{\partial x_j \partial x_j} \tag{2.2}$$

The same numerical approach as used in Jiang et al. (2016) is adopted here. Specifically, the FVM approach and the PISO (Pressure Implicit with Splitting of Operators) algorithm (Issa, 1986) are used to solve the equations. The convection, diffusion and time derivative terms are discretized, respectively, using a fourth-order cubic scheme, a second-order linear scheme, and a blended scheme consisting of the second-order Crank-Nicolson scheme and a first-order Euler implicit scheme.

2.2. Computational domain and mesh

The computational domain and mesh are determined based on a domain size and mesh resolution dependence study reported separately in Jiang et al. (2016). The standard 3D mesh reported in Jiang et al. (2016) is adopted in this study. Based on the standard 3D mesh, Jiang et al. (2016) obtained DNS results of wake transitions of a circular cylinder which are in good agreement with the experimental results reported in Williamson (1996).

The details of the standard 3D mesh are as follows. A hexahedral computational domain of $50D \times 40D \times L_z$ as shown in Fig. 1(a) is constructed. The spanwise domain length L_z is varied in this study. In the x-y plane (i.e. the plane perpendicular to the cylinder span), the cylinder perimeter is discretized with 132 nodes. The radial size of the first layer of mesh next to the cylinder is $0.001D$. The cell expansion ratio in the whole domain is kept below 1.1. For wake structure visualization, a relatively high

mesh resolution in the near wake is used by specifying a constant cell size along the x-direction for x/D ranges from approximately 1.0 to 5.5. A close-up view of the mesh in the x-y plane near the cylinder is shown in Fig. 1(b). The 3D mesh is formed by replicating the two-dimensional (2D) mesh along the z-axis, resulting in an identical mesh resolution in all planes perpendicular to the cylinder span. The cell size in the spanwise direction is $0.1D$.

The boundary conditions are specified as follows. At the inlet boundary, a uniform flow velocity U is specified in the x-direction. At the outlet, the Neumann BC (i.e. zero normal gradient) is applied for the velocity, and the pressure is specified as a reference value of zero. The symmetry BC is applied at the top and bottom boundaries. The non-slip BC is applied on the cylinder surface. At the two lateral boundaries perpendicular to the cylinder span, both the periodic and the symmetry BCs are tested in this study. The periodic BC is used by default unless otherwise stated.

3. Prediction of Re_{cr}

3.1. Influence of λ on the prediction of Re_{cr}

It is found that the prediction of Re_{cr} is affected by the accuracy of the spanwise wavelength simulated by DNS (based on the choices of the lateral BC and L_z). This is explained with reference to the neutral stability curve for Mode A as presented by Barkley and Henderson (1996) and Posdziech and Grundmann (2001) (partially reproduced in Fig. 2 for the convenience of discussion). Note that the vertical coordinate λ shown in Fig. 2 refers to the wavelength of perturbations. According to Barkley and Henderson (1996), flow past a circular cylinder is linearly unstable to 3D perturbations only if the wavelength of perturbations falls in the area enclosed by the neutral curve at the corresponding Re value. The dashed line that cuts through the enclosed area represents the variation of λ_A with Re. The points on the neutral curve correspond to the neutral state of the flow where perturbations neither grow nor decay.

For numerical simulations, the maximum wavelength of perturbations is capped by L_z. A direct interpretation is that no Mode A instability would be triggered if L_z is

smaller than the corresponding λ on the lower branch of the neutral curve for the periodic lateral BC (Fig. 2) or $L_z < \lambda/2$ for the symmetry lateral BC. If the wavelength of perturbations contained in the numerical simulation falls within the area enclosed by the neutral curve (Fig. 2), Mode A instability would be triggered. Since the spanwise wavelength λ of the flow predicted by DNS is determined by the choices of the lateral BC and L_z, while Re_{cr} is normally determined by trial and error through varying Re along a constant value of λ, the predicted Re_{cr} would be the corresponding Re value at the intersection point of the neutral curve with the horizontal line passing through λ (rather than λ_A). It is seen from Fig. 2 that Re_{cr} would inevitably be over-predicted if the simulated spanwise wavelength λ of the Mode A structure is different from the intrinsic wavelength λ_A at the left tip of the neutral curve, regardless of under- or over-prediction of λ.

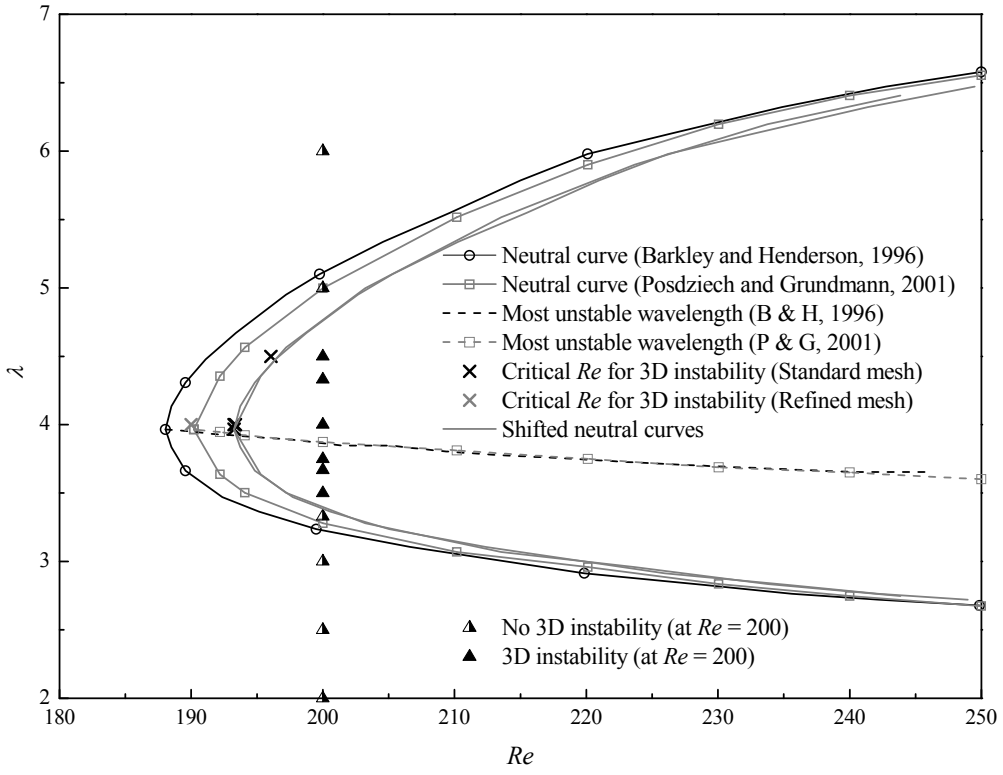

Fig. 2. Dependence of the 3D Mode A wake instability on the spanwise wavelength and the Reynolds number (with the periodic lateral BC).

This potential issue was less considered in previous 3D DNS studies for the

prediction of Re_{cr}. Table 1 lists some studies on the prediction of Re_{cr}, along with their choices of the lateral BC and L_z. It is found that apart from Jiang et al. (2016), the predicted Re_{cr} values were all larger than the ones obtained from the linear stability analysis (e.g. 188.5 (±1.0) by Barkley and Henderson (1996), 190.2 (±0.02) by Posdziech and Grundmann (2001), and 190.5 by Rao et al. (2013)) and the experimental study (e.g. Re_{cr} = 194 by Williamson (1996)). The relatively accurate prediction of Re_{cr} by Jiang et al. (2016) was achieved with the periodic lateral BC and L_z = 12.0. In that case, three Mode A streamwise vortex pairs were observed along the cylinder span width, which resulted in a simulated λ of 4.0 that is very close to the λ_A of 3.96 (Barkley and Henderson, 1996) or 3.966 (Posdziech and Grundmann, 2001) at the left tip of the neutral curve (Fig. 2). In contrast, the discrepancy between λ and λ_A for some other studies listed in Table 1 would contributed to the over-prediction of Re_{cr}.

Table 1. Prediction of Re_{cr} based on different choices of the lateral BC and L_z.

Reference	Method	Lateral BC	L_z	Simulated λ	Predicted Re_{cr}
Karniadakis and Triantafyllou (1992)	SEM	Periodic	π, 2π	π	200 – 210
Behara and Mittal (2010)	FEM	Symmetry	10.0	4.0	200
Zhao et al. (2013)	FEM	Periodic	19.2	3.84	> 200
Tong et al. (2014)	FVM	Symmetry	9.6	3.84	> 200
Jiang et al. (2016)	FVM	Periodic	12.0	4.0	193.25

In addition to the influence by λ, the mesh resolution in the *x*-*y* plane is also an important factor affecting the prediction of Re_{cr}. For example, based on a refined 3D mesh with four times the cell number in the *x*-*y* plane with respect to the standard 3D mesh, a slightly reduced and converged Re_{cr} value of 189.96 is obtained, which is

extremely close to the linear stability analysis result of Re_{cr} ~ 190 and ~1.7% smaller than the Re_{cr} of 193.25 obtained with the standard 3D mesh. To facilitate comparison of the present DNS results based on the standard 3D mesh with the linear stability analysis results, the influence of the mesh resolution on the prediction of Re_{cr} is taken into account by translating the left tips of the two neutral curves by Barkley and Henderson (1996) and Posdziech and Grundmann (2001) horizontally to Re = 193.25 while maintaining the same increase rate of Re for all of the points on each curve (Fig. 2). It is also seen that the two shifted neutral curves are in better agreement with each other than before (Fig. 2). It is believed that this is also due to the elimination of the mesh dependence effect of the results between Barkley and Henderson (1996) and Posdziech and Grundmann (2001).

3.2. Prediction with the periodic lateral BC

Recall that the L_z (= 12) used in Jiang et al. (2016) corresponds to a λ (= 4.0) that is marginally larger than λ_A (= 3.96 or 3.966). Further calculation is carried out to assess the influence of the ~ 1% discrepancy between λ and λ_A on the accuracy of the prediction of Re_{cr}. The calculation is performed with the standard 3D mesh and L_z = 11.9. This corresponds to λ = 3.967 which is extremely close to the λ_A obtained from linear stability analysis (with a discrepancy of ~ 0.1%). The Re_{cr} value obtained with L_z = 11.9 is 193.26, which is extremely close to the Re_{cr} of 193.25 obtained with L_z = 12.0 (λ = 4.0) in Jiang et al. (2016). It is seen that a 1% discrepancy between λ and λ_A induces a negligible difference on the prediction of Re_{cr}. This is because that Re_{cr} is relatively insensitive to the variation of λ at the left end of the neutral curve (Fig. 2).

Furthermore, simulations are carried out with L_z = 4.0, 8.0 and 24.0 which ultimately lead to a λ of 4.0. The Re_{cr} values obtained with L_z = 4.0, 8.0 and 24.0 are 193.39, 193.37 and 193.35, respectively. The above cases demonstrate that the prediction of Re_{cr} is negligibly influenced by the absolute span length of the computational domain as long as the simulated λ is accurate enough.

In contrast, a much higher Re_{cr} of 196.05 is obtained with L_z = 13.5. This is

because L_z = 13.5 leads to an inaccurate prediction of λ = 4.5 which is ~ 13.6% larger than λ_A. The predicted Re_{cr}, although on the shifted neutral curves shown in Fig. 2, is not at the left tip and therefore not accurate. This case confirms that the discrepancy between λ and λ_A contributes to the over-prediction of Re_{cr} in 3D DNS. For an accurate prediction of Re_{cr}, it is essential to choose a proper L_z which satisfies the criterion of $\lambda = \lambda_A$.

To further examine the influence of L_z on the simulation results, a series of cases at Re = 200 is calculated, with L_z ranging from 1 to 16. It is found that 3D instability does not occur (i.e. $Re_{cr} > 200$) for L_z = 1, 2, 3, 5, 6, and 10. For the cases with 3D instability, the simulated wavelength of Mode A is plotted in Fig. 2. For the cases without 3D instability, all the possible wavelengths ($\lambda = L_z/n$) are plotted in Fig. 2. It is seen that the two groups of the wavelengths are well separated by the shifted neutral curves, which once again confirms the over-prediction of Re_{cr} due to the influence of λ.

The influence of L_z on the prediction of Re_{cr} is further explained in Fig. 3 where the shifted neutral curve from Barkley and Henderson (1996) is transformed into the (Re, L_z) space by employing $L_z = n\lambda$. Neutral curves with n = 1 – 6 are plotted in Fig. 3. The left tip of each of the neutral curves is placed at (Re_{cr}, $n\lambda_A$) = (193.25, 3.96n). The shadow area in Fig. 3 represents the parameter range within which 3D instability does not occur, while 3D instability is expected to be observed in the clear area. This is confirmed by the numerical results with Re = 200 as shown in Fig. 3. It is also seen that all the points located at the left tip of the neutral curves which satisfy $L_z \sim n\lambda_A$ correspond to the lowest and most accurate Re_{cr} values.

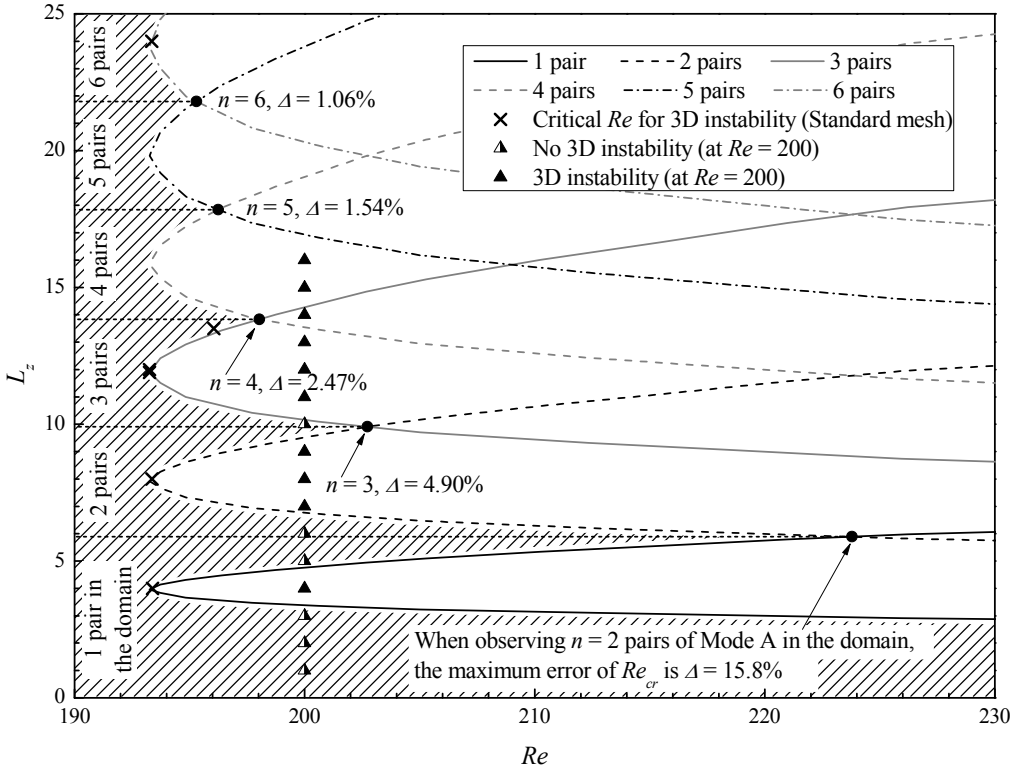

Fig. 3. Dependence of the 3D Mode A instability on the spanwise domain length and the Reynolds number (with the periodic lateral BC).

It is expected that the maximum relative error in the prediction of Re_{cr} generally decreases with increase of L_z (but not monotonically). Since 3D instability would not be observed in the shadow area of Fig. 3, the best estimate of Re_{cr} that can be obtained for a given L_z corresponds to the intersection point between a horizontal line through L_z and the neutral curve. If Fig. 3 is separated into a number of horizontal strips by drawing horizontal dashed lines through the intersection points (marked by solid dots) of the adjacent neutral curves, the horizontal strip that encloses (Re_{cr}, $n\lambda_A$) represents a parameter space within which n pairs of the Mode A structure are expected. For a particular L_z value that falls into the horizontal strip that encloses (Re_{cr}, $n\lambda_A$), the maximum difference between the predicted Re_{cr} and the real Re_{cr} is bounded by the difference between the Re value corresponding to the dot point at the lower boundary of the horizontal strip and the real Re_{cr} value if $L_z < n\lambda_A$, and the difference between the Re value corresponding to the dot point at the upper boundary of the horizontal strip and the real Re_{cr} value if $L_z > n\lambda_A$. For example, for $n = 2$ the maximum relative

errors (Δ) of the prediction of Re_{cr} for $L_z < 2\lambda_A$ and for $L_z > 2\lambda_A$ are 15.8% and 4.9%, respectively. It is seen from Fig. 3 that the maximum relative error reduces when more Mode A vortex pairs are resolved in the domain. If λ_A is not known *a priori*, the resolution of 3 pairs of Mode A in the domain generally indicates a relative error of less than 5% in the prediction of Re_{cr}, and the resolution of 6 pairs of Mode A generally indicates a relative error of less than 1%.

3.3. Influence of the lateral BC on the prediction of Re_{cr}

The influence of L_z on the prediction of Re_{cr} and λ for the symmetry lateral BC is examined by conducting a series of numerical tests at $Re = 200$. For each combination of the lateral BC and L_z, the possible λ values for Mode A ($\lambda = L_z/n$ for the periodic BC and $\lambda = 2L_z/n$ for the symmetry BC) and the simulated λ are both shown in Fig. 4. The possible values below $\lambda = 2$ are omitted for simplicity. For the cases without 3D instability, the simulated λ is regarded as ∞ in Fig. 4. The shadow area in Fig. 4 represents the range of λ enclosed by the shifted neutral curves within which 3D instability is expected. It is seen that outside this range, 3D instability cannot be excited. Since there are more chances that the possible λ falls into the neutral curve range for a given L_z by using the symmetry BC than the periodic BC, it is more likely for the flow to form a 3D instability by using the symmetry BC. This is consistent with the results shown in Fig. 3 (for the periodic BC) and Fig. 5 (for the symmetry BC). In Fig. 5, in addition to $L_z = n\lambda$, the neutral curves are also transformed to $L_z = (n - 0.5)\lambda$. It is seen that the use of the symmetry BC leads to a reduction of error in the prediction of Re_{cr}. For example, if λ_A is not known *a priori*, the resolution of 3 pairs of Mode A with the symmetry BC (rather than 6 pairs with the periodic BC) generally indicates a relative error of less than 1% in the prediction of Re_{cr} (Fig. 5).

Fig. 6 shows the relative errors in the prediction of Re_{cr} as a function of L_z. Judging from the fitted curves based on the local peaks of the relative errors, the maximum relative error one can expect by using the symmetry BC is less than a half of that from using the periodic BC at the same L_z value.

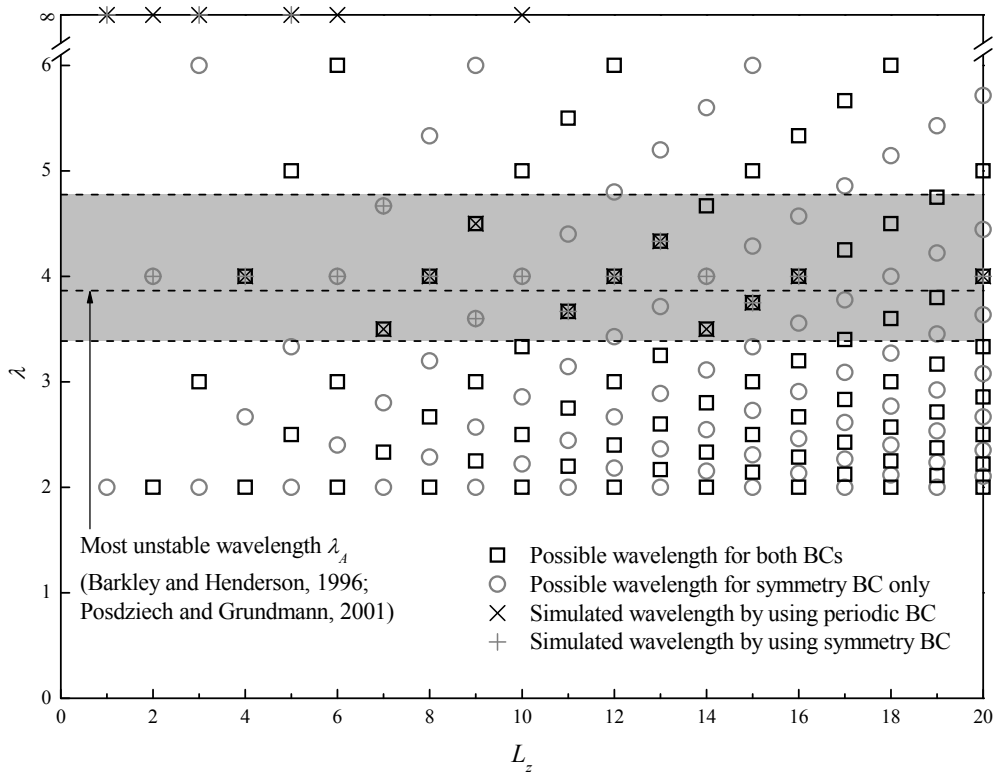

Fig. 4. Possible λ values for Mode A and the simulated λ for each lateral BC and L_z combination.

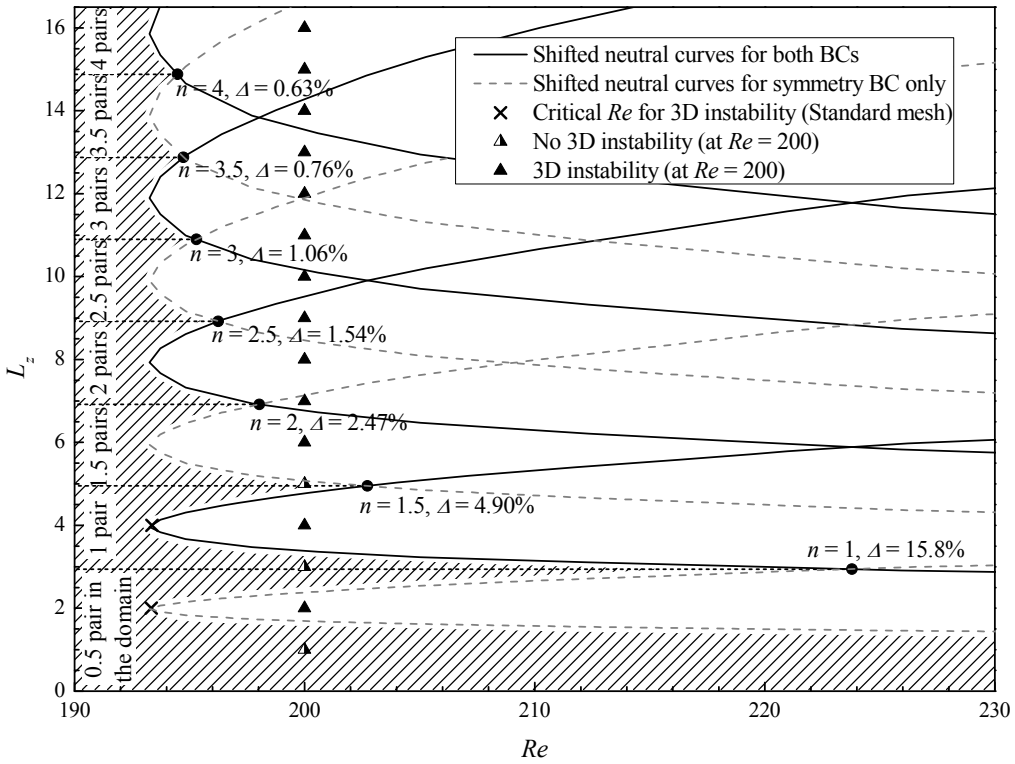

Fig. 5. Dependence of the 3D Mode A instability on the spanwise domain length and the Reynolds number (with the symmetry lateral BC).

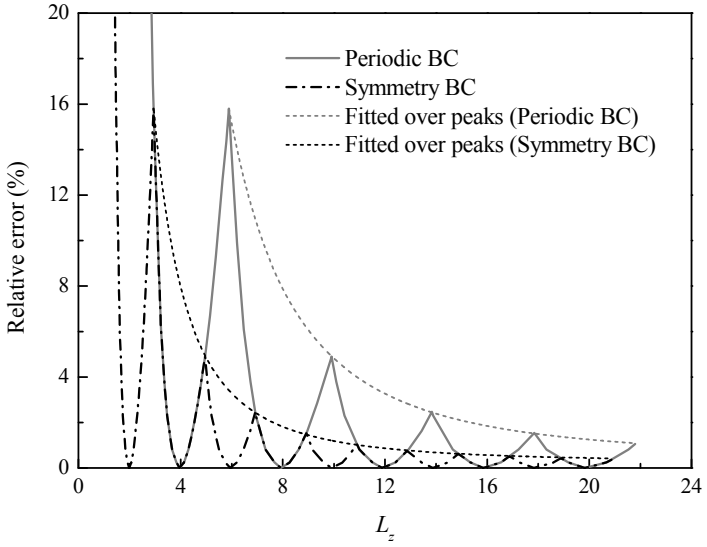

Fig. 6. Relative error in the prediction of Re_{cr} as a function of L_z.

It has been demonstrated previously by using the periodic BC that an accurate prediction of Re_{cr} requires $\lambda = \lambda_A$ rather than a long L_z. This is also confirmed by using the symmetry BC and low L_z values of 2.0 and 4.0 (both correspond to $\lambda = 4.0$). The predicted Re_{cr} are 193.33 and 193.37, respectively, close enough to the ones obtained with the periodic BC and $\lambda = 4.0$. For the purpose of minimizing the computational cost while maintaining the accuracy of the prediction of Re_{cr}, the use of the symmetry BC and $L_z = \lambda_A/2$ (if λ_A is known *a priori*) is recommended. The simulation of only a half of a pair of the Mode A structure is guaranteed by the antisymmetrical nature of the Mode A vortex pairs.

4. Prediction of the 3D wake flow at *Re* = 200

4.1. Hydrodynamic forces and flow three-dimensionality

The previous set of cases at $Re = 200$ (just above Re_{cr}) with $L_z = 1 – 16$ and both lateral BCs is further used to investigate the influence of the lateral BC and L_z on the prediction of the wake structures and hydrodynamic forces on the cylinder. The

influence on the vortex structures (including the development of vortex dislocations) is examined through numerical flow visualization of the non-dimensional streamwise vorticity:

$$\omega_x = \left(\frac{\partial u_z}{\partial y} - \frac{\partial u_y}{\partial z} \right) \frac{D}{U} \tag{4.1}$$

The three-dimensionality of the flow is quantified by the spanwise disturbance energy E_z (divided by L_z to facilitate comparison) which is defined as:

$$E_z = \frac{1}{2L_z} \int_V \left(\frac{u_z}{U} \right)^2 \mathrm{d}V \tag{4.2}$$

where V is the non-dimensional volume of the flow field of interest (the near-wake region of x/D = 0 – 5, y/D = -20 – 20, and z/D = 0 – L_z for the present study). The fully developed flow is also quantified by examining the Strouhal number (St), the base pressure coefficient (C_{pb}), and the drag and lift force coefficients (C_D and C_L), which are defined as:

$$St = f_L D / U \tag{4.3}$$

$$C_{pb} = (p_b - p_\infty) / (\rho U^2 / 2) \tag{4.4}$$

$$C_D = F_D / (\rho D U^2 L_z / 2) \tag{4.5}$$

$$C_L = F_L / (\rho D U^2 L_z / 2) \tag{4.6}$$

where f_L is the frequency of the fluctuating lift force, p_b is the time-averaged pressure at the rear stagnation point of the cylinder, p_∞ is the reference pressure at the inlet of the domain, ρ is fluid density, and F_D and F_L are the integrated drag force and lift force on the cylinder, respectively. The time-averaged drag and lift coefficients are denoted as $\overline{C_D}$ and $\overline{C_L}$, respectively. The root-mean-square lift coefficient C_L' is defined as:

$$C_L' = \sqrt{\frac{1}{N} \sum_{i=1}^{N} \left(C_{L,i} - \overline{C_L} \right)^2} \tag{4.7}$$

where N is the number of values in the time-history of C_L.

The present numerical results show that the choices of the lateral BC and L_z do

have some effects on the wake structures. For example, for the cases of P4 and S4 (the letter P or S represents the periodic (P) or symmetry (S) lateral BC while the number denotes the chosen L_z), the cylinder wake is exclusively occupied by one pair of sustained Mode A vortex structure which contains some small-scale irregularities. A typical streamwise vorticity field for the case of P4 is shown in Fig. 7(a), where a small-scale irregularity is marked by the rectangular frame. For the case of S2, a half of the vortex pair is observed. However, vortex dislocation is completely suppressed due to the confinement of the short span. This is consistent with the numerical results by Henderson (1997) and Persillon and Braza (1998) by using short span lengths. Due to the absence of dislocation, the fluctuations of the drag and lift coefficients in the fully developed state are quite regular (Fig. 8(a)), and the spanwise energy E_z remains in an equilibrium level without large-amplitude fluctuations (Fig. 8(b)). As can be seen in Fig. 8, the reductions of the drag coefficient and the fluctuation amplitude of the lift coefficient from their 2D counterparts (marked by the horizontal dashed lines in Fig. 8(a)) are consistent with the increase of E_z. These variations indicate that the energy is partly transferred to the spanwise direction.

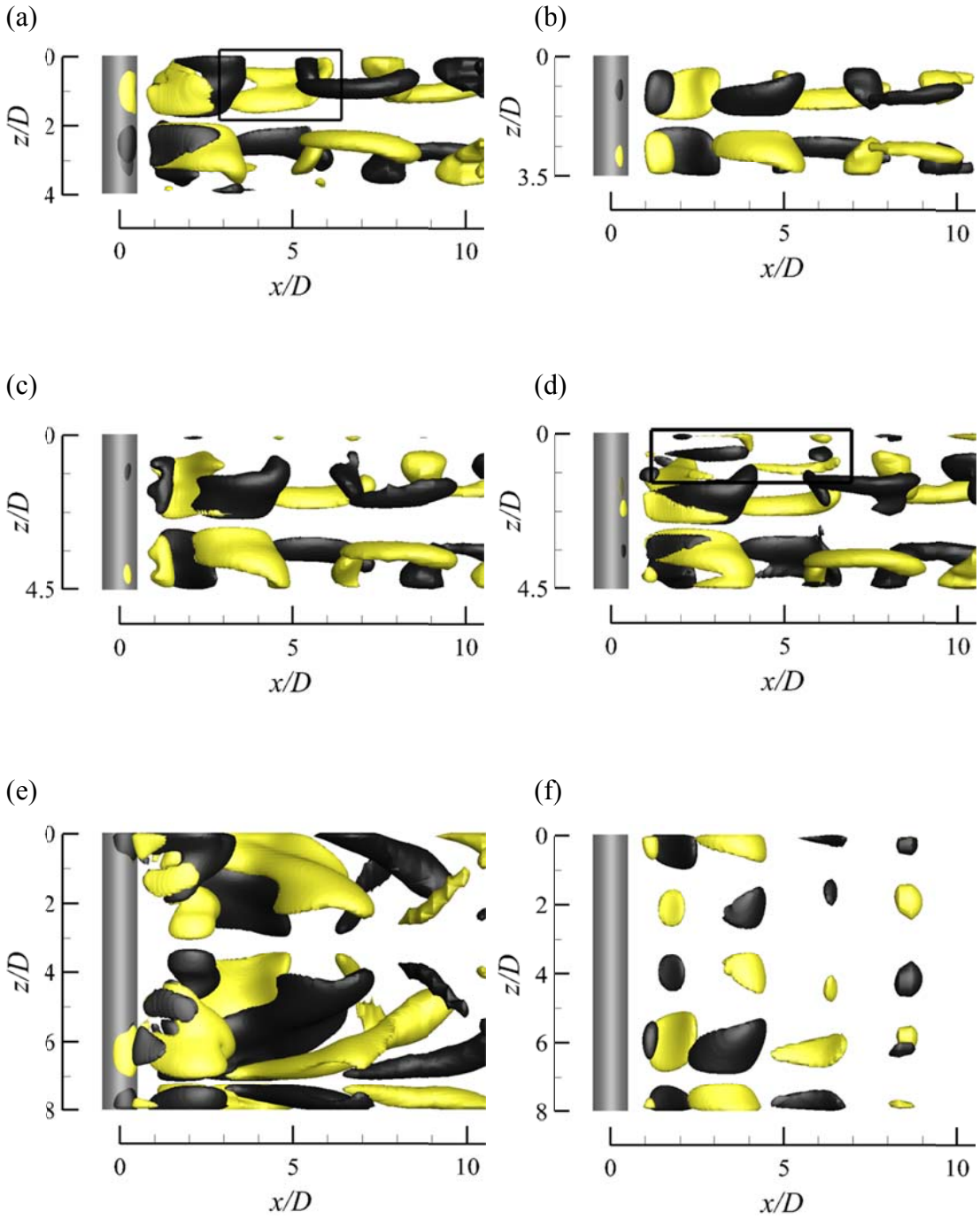

Fig. 7. Iso-surfaces of $\omega_x = \pm 0.5$ at $Re = 200$: (a) case P4 at $t^* = 2550$ (Mode A with small-scale irregularities), (b) case P3.5 at $t^* = 1400$ (ordered Mode A), (c) case P4.5 at $t^* = 940$ (ordered Mode A), (d) case P4.5 at $t^* = 1000$ (with small-scale vortex dislocations), (e) case P8 at $t^* = 2480$ (with large-scale vortex dislocations), and (f) case P8 at $t^* = 2580$ (ordered Mode A). Dark grey and light yellow denote positive and negative values, respectively. The flow is from the left to the right past the cylinder on the left.

(a)

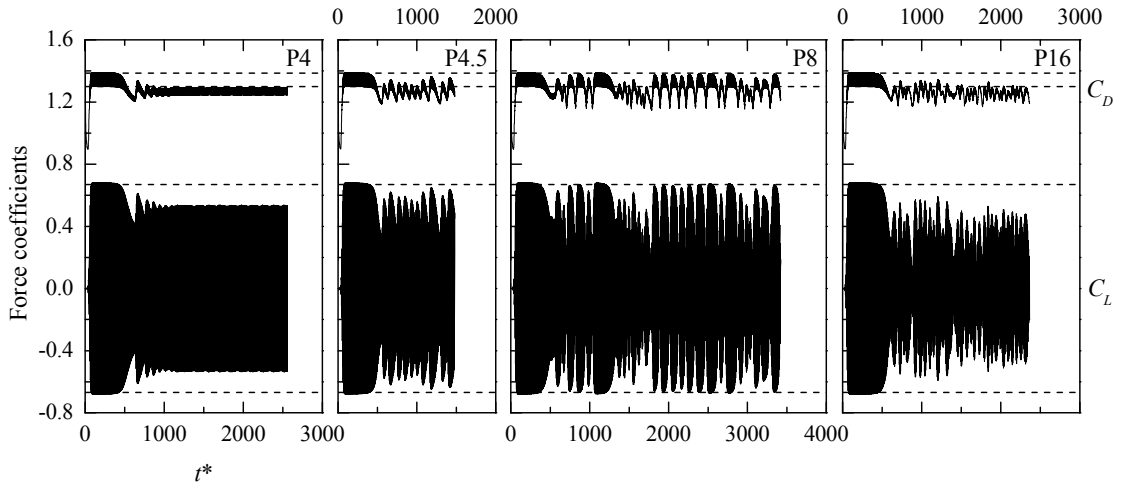

(b)

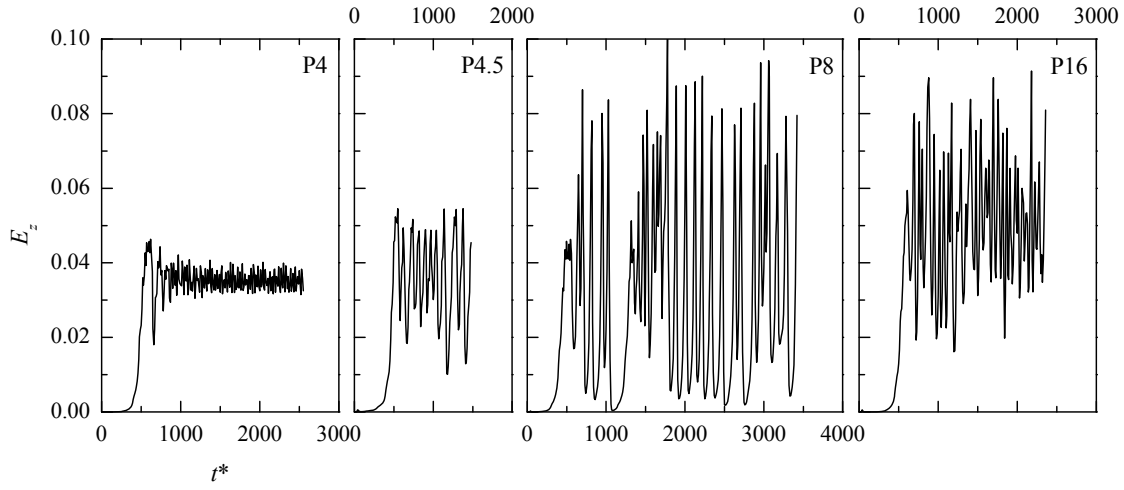

Fig. 8. Time-histories of (a) the drag and lift coefficients, and (b) the spanwise disturbance energy integrated over x/D = 0 – 5, for the cases with different L_z (with the periodic lateral BC). The horizontal dashed lines denote the fluctuation amplitudes of the force coefficients obtained with 2D DNS.

Further calculations with L_z = 3.5 (= 0.906λ_A), 3.865 (= λ_A), 4.2 (= 1.087λ_A), and 4.5 (= 1.164λ_A) are carried out. For each of the above L_z, almost identical results are obtained by using the two lateral BCs. Similar results as discussed in the previous paragraph by using L_z = 4.0 are also observed for L_z = 3.865 and 4.2. However, due to a stronger confinement by using L_z = 3.5 (< λ_A), the Mode A vortex pair becomes

extremely ordered (Fig. 7(b)). For a less confined L_z of 4.5, alternate formation of the relatively ordered Mode A structure (Fig. 7(c)) and small-scale vortex dislocations (marked by a rectangular frame in Fig. 7(d)) can be observed. Consequently, irregular fluctuations of the time-histories of the force coefficients and E_z are observed in the fully developed state (Fig. 8). It should be noted that for L_z within the range of 3.387 to 4.774 which includes all of the above cases, only one pair of the Mode A structure is expected at the onset of the secondary instability (see Fig. 3 and Fig. 5). However, according to the above case studies, the upper limit of L_z for the complete suppression of vortex dislocation is ~ $1.1\lambda_A$ ($4.2 < L_z < 4.5$) rather than $L_z = 4.774$. This indicates that the suppression of dislocation is due to the confinement of L_z to the intrinsic wavelength λ_A, rather than the initial formation of only one pair of Mode A.

Beyond $L_z \sim 1.1\lambda_A$, dislocations can be observed and the time-histories of the force coefficients and E_z display irregular fluctuations. However, for $1.1\lambda_A < L_z \leq 9$, dislocations in the domain may disappear completely once in a while, and be replaced by the development of extremely ordered Mode A structure. This is illustrated with the case of P8 as shown in Fig. 7(e) (with large-scale vortex dislocations) and Fig. 7(f) (ordered Mode A). The disappearance of the dislocations results in a dramatic reduction of the flow three-dimensionality in the domain. As shown in the third column of Fig. 8, the fluctuation amplitudes of the force coefficients can once in a while reach their 2D counterparts and meanwhile the E_z value exhibits a sharp drop to a very low level. As the ordered Mode A starts to develop after that, the flow three-dimensionality starts to grow again. This phenomenon is most pronounced in P9 and P8 where the time-averaged E_z decreases significantly compared with the rest of the cases (Fig. 9).

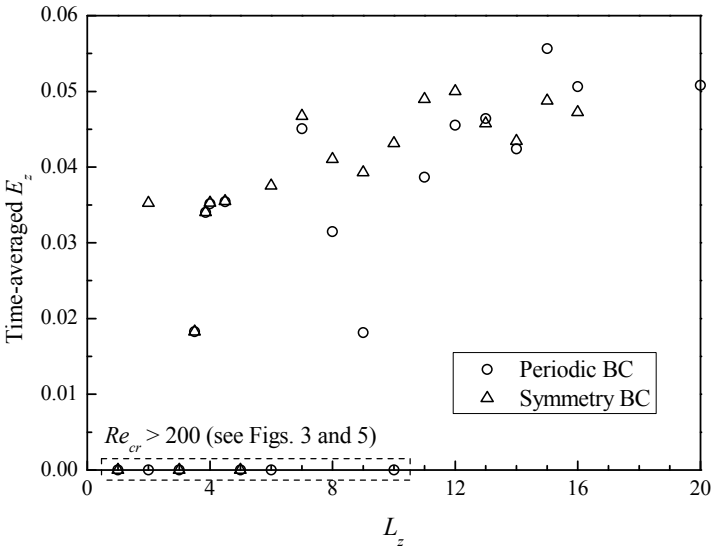

Fig. 9. Time-averaged spanwise energy E_z integrated over the near wake region of x/D = 0 – 5.

Fig. 10 shows the statistically stationary hydrodynamic forces on the cylinder calculated from the fully developed flow. For the cases without 3D instability, 500 non-dimensional time units (defined as $t^* = Ut/D$) are used for the statistics. The statistically stationary results are very close to the 2D DNS results as marked in Fig. 10, and are thus omitted for simplicity. When 3D instability takes place, 800 to 1000 non-dimensional time units are used for the statistics. The sufficiency of the statistical data is confirmed by obtaining very close results with only the second half of the sampling period (see Fig. 10).

(a)

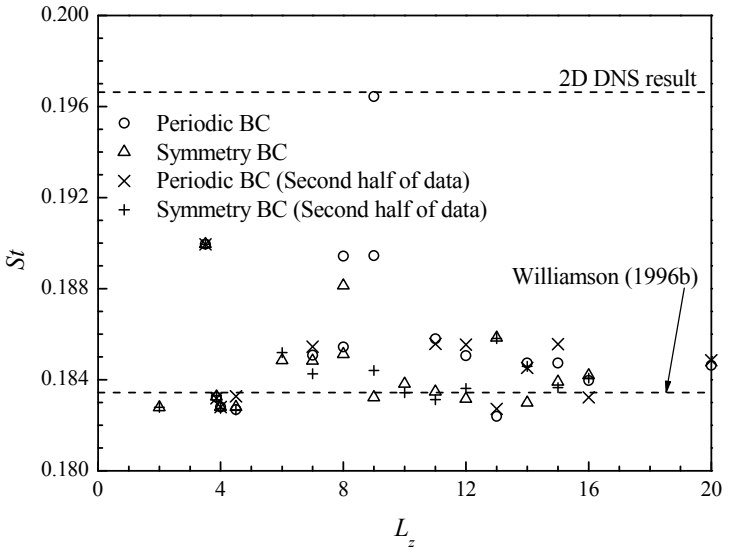
0.200
0.196
0.192
0.188
0.184
0.180
St
2D DNS result
Periodic BC
Symmetry BC
Periodic BC (Second half of data)
Symmetry BC (Second half of data)
Williamson (1996b)
0
4
8
12
16
20
L_z

(b)

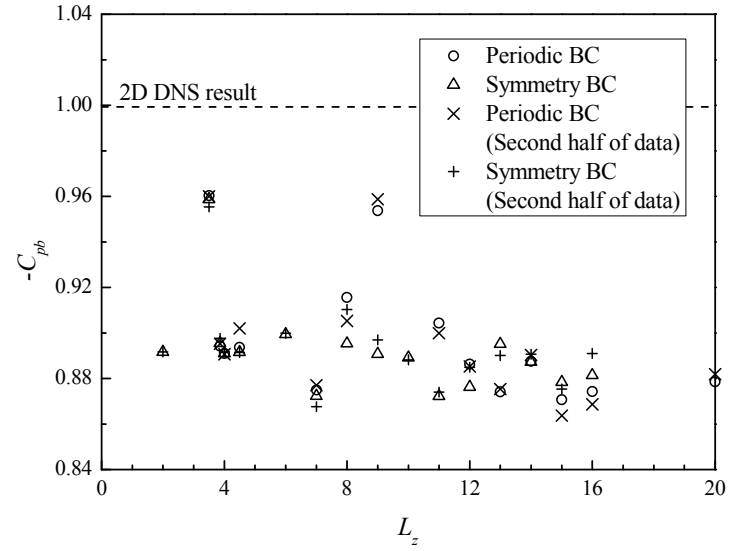
1.04
1.00
0.96
0.92
0.88
0.84
$-C_{pb}$
2D DNS result
Periodic BC
Symmetry BC
Periodic BC
(Second half of data)
Symmetry BC
(Second half of data)
0
4
8
12
16
20
L_z

(c)

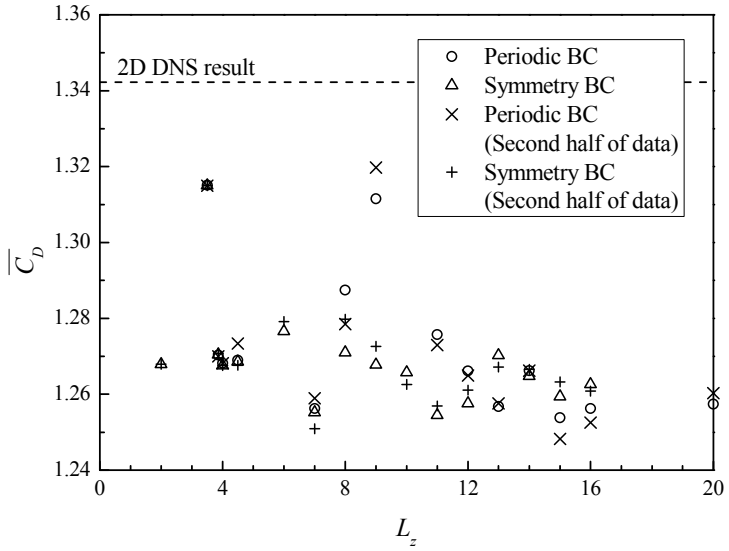
1.36
1.34
1.32
1.30
1.28
1.26
1.24
$\overline{C_D}$
2D DNS result
Periodic BC
Symmetry BC
Periodic BC
(Second half of data)
Symmetry BC
(Second half of data)
0
4
8
12
16
20
L_z

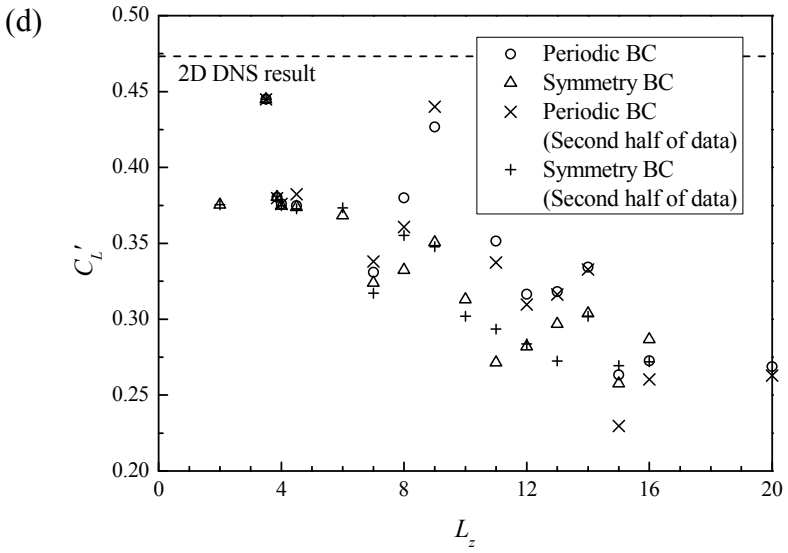

Fig. 10. Statistically stationary hydrodynamic forces on the cylinder: (a) the Strouhal number, (b) the base pressure coefficient, (c) the mean drag coefficient, and (d) the root-mean-square lift coefficient. The results obtained with the periodic BC are shown by open circles (○) while the results obtained with the symmetry BC are shown by open triangles (△). To confirm the sufficiency of the statistical data, the results obtained with only the second half of the sampling period are shown by (×) for the periodic BC and (+) for the symmetry BC.

In Fig. 10(a), *St* is determined based on the peak frequency derived from the fast Fourier transform (FFT) of the time-history of C_L. Normally, a distinct peak frequency is observed, which corresponds to a single *St* value. However, a distinct peak frequency is not observed for the cases of P8, P9, and S8 even when the calculation is performed up to 3500 non-dimensional time units. Hence the *St* values corresponding to the two leading peaks are plotted in Fig. 10(a). For the case of P9, one of the leading frequencies even reaches the 2D limit, and the base pressure and force coefficients shown in Fig. 10(b–d) are also obviously over-predicted. This is due to the frequent disappearance of the vortex dislocations as discussed earlier on.

Apart from the cases of P8, P9, and S8 for which temporal complexity is observed for the fully developed flow, the cases with $L_z > 9$ all produce similar results of *St*, C_{pb}, and $\overline{C_D}$. The small discrepancy ranges of the results (1.9%, 3.8%, and

1.7%, respectively) are largely attributed to the limited sampling periods. In contrast, a roughly decreasing trend of C_L' is observed with increasing L_z. As addressed by Henderson (1997), this is because the integrated lift coefficient is more likely to be cancelled out by the phase differences along the span. According to the above results, $L_z > 10$ is required to accurately predict the hydrodynamic forces on the cylinder (apart from the ones that may be cancelled out along the span). Surprisingly, even without the occurrence of vortex dislocation, the use of $L_z = \lambda_A$ can also give fairly close approximations of St, C_{pb}, and $\overline{C_D}$. However, under the even stronger confinement of $L_z \sim 0.9\lambda_A$ where only extremely ordered Mode A takes place, the three-dimensionality of the flow is drastically reduced, which is represented by the obvious shifts of the E_z and hydrodynamic forces towards the 2D limit (Fig. 9 and Fig. 10).

4.2. Distribution of the vortices in the spanwise direction

Although similar quantitative results such as the E_z and hydrodynamic forces are obtained by using the periodic and symmetry BCs, the distribution of the vortices along the cylinder span can be different. According to the symmetry BC assumption given in Eq. (1.5), the streamwise vorticity ω_x and the transverse vorticity ω_y (= $\partial u_x/\partial z - \partial u_z/\partial x$) are both forced to be zero at the two lateral boundaries perpendicular to the span. As a result, the development of the ω_x and ω_y components near the two lateral boundaries is restricted. One example is that oblique vortex shedding would be completely suppressed at the two ends of the span by the symmetry BC.

Fig. 11 shows the spanwise distribution of the time-averaged spanwise disturbance $(u_z/U)^2$ sampled at $(x/D, y/D) = (3.0, 0.5)$ along the cylinder span. The sampling periods are the same as those used for obtaining the E_z and hydrodynamic forces. Similar results as shown in Fig. 11 are also observed for the spanwise distribution of the time-averaged streamwise enstrophy ω_x^2 sampled at the same point along the span. Hence the results of ω_x^2 are not presented and only the results of $(u_z/U)^2$ are discussed.

It is seen in Fig. 11 that for all of the cases using the symmetry BC, the $(u_z/U)^2$ at the two ends of the span decreases to zero. This also restricts the development of flow three-dimensionality and vorticity for at least 0.5D from each end of the span. In contrast, the periodic BC is free from this restriction, and the $(u_z/U)^2$ does not drop to very small values at any position along the span width for $L_z > 10$.

For the cases of P4 and S4, two extremely regular peaks of the $(u_z/U)^2$ are observed along the cylinder span (Fig. 11). This is because only one pair of sustained Mode A vortex structure (without dislocation) is observed in the domain (Fig. 7(a)) and it does not vary along the span. For the cases with $L_z = 7 – 9$, dislocations can be observed for more than 70% of the sampling period (apart from ~ 35% for P9), yet the flow three-dimensionality and vortices distributed along the span width are still strongly affected by the insufficiency of L_z. Under the symmetry BC, the spanwise distribution of the $(u_z/U)^2$ is largely symmetrical for S6, S7, and S9. Under the periodic BC, a periodic spanwise distribution of the $(u_z/U)^2$ is observed for P7. In addition, the $(u_z/U)^2$ may even drop to extremely low levels (apart from the two ends of the span) for S6, S7, P7, P8, and P9, which suggests that dislocations are not randomly distributed along the span but are actually avoiding some particular spanwise locations. For both lateral BCs, randomly distributed dislocations can only be achieved with $L_z > 10$.

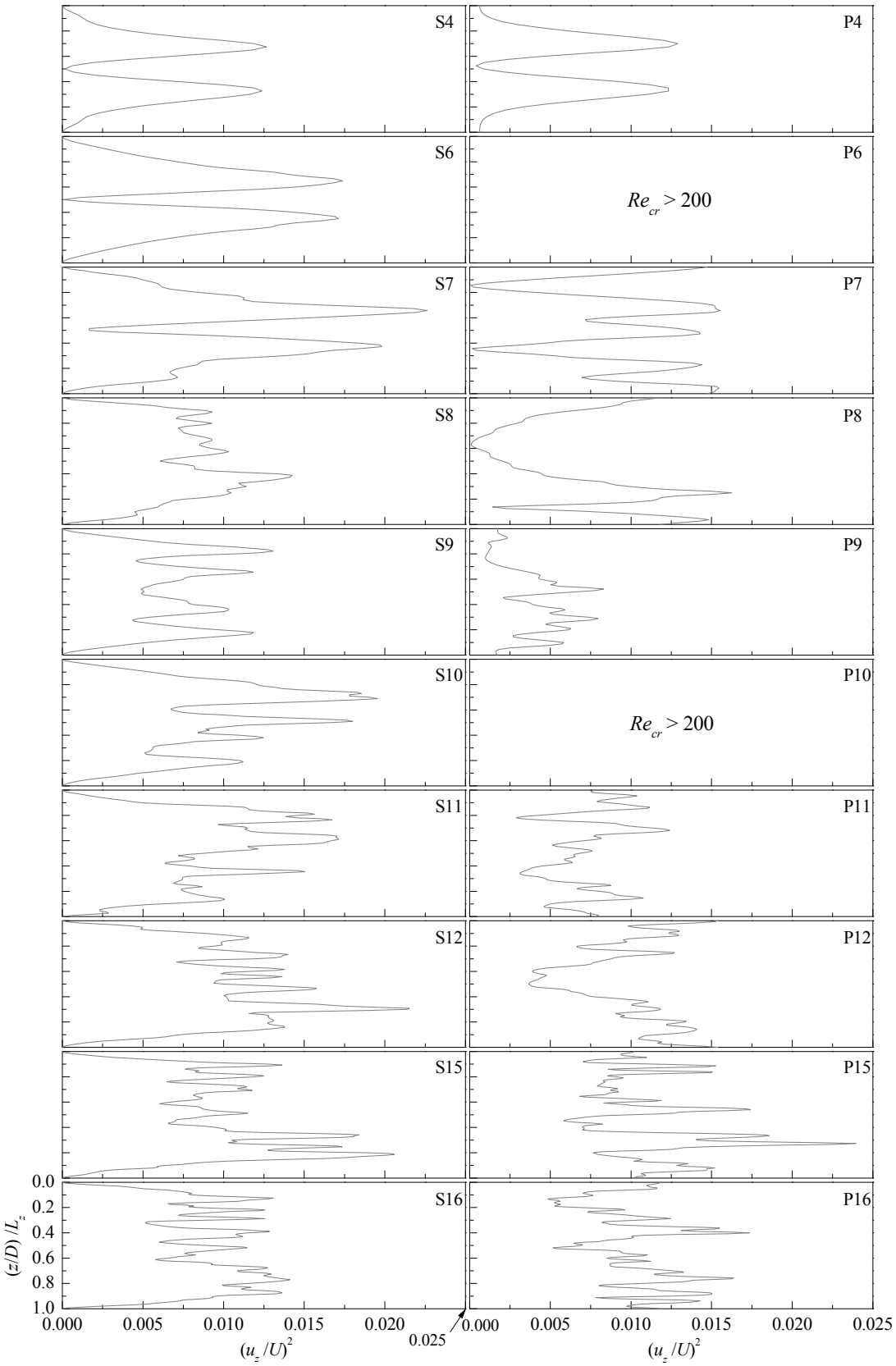

Fig. 11. Spanwise distribution of the time-averaged spanwise disturbance $(u_z/U)^2$ sampled at (x/D, y/D) = (3.0, 0.5) along the cylinder span for the cases with different

L_z and lateral BCs.

5. Influence of the intrinsic wavelengths for $Re > Re_{cr}$

Apart from leading to an over-prediction of Re_{cr}, the difference between the simulated wavelength λ and the most unstable wavelengths λ_A and λ_B may also affect the simulation results in the subsequent wake transition stages, including Mode A with large-scale vortex dislocations ($Re_{cr} < Re \leq 260$), the mode swapping process ($230 \leq Re \leq 260$), and the occurrence of relatively ordered Mode B ($265 \leq Re \leq 270$) and disordered Mode B structures ($Re \geq 280$). The above ranges of Re were obtained by Jiang et al. (2016) based on the same numerical formulation and computational mesh (with the periodic lateral BC and $L_z = 12$).

Previous numerical studies simulating the 3D flows adopted different criteria for the choice of L_z. The SEM studies by Henderson (1997) and Posdziech and Grundmann (2001) specified L_z to be very close to an integer multiple of λ_A and λ_B, since they believed that for an accurate prediction of the 3D results the largest Mode A and Mode B eigenvalues in the discrete spectrum should be included. On the other hand, some studies using the conventional 3D DNS involving FEM and FVM formulations adopted a constant L_z for the cases with different Re (e.g. Persillon and Braza, 1998; Behara and Mittal, 2010; Zhao et al., 2013; Tong et al., 2014), irrespective of the reduction of λ_A with increases of Re as reported by Williamson (1996) and Barkley and Henderson (1996).

The effect of the discrepancy between the simulated wavelength λ (based on the lateral BC and L_z) and the intrinsic most unstable wavelengths λ_A and λ_B on the 3D DNS results for $Re > Re_{cr}$ is examined. Section 4 presents the results at $Re = 200$ which falls into the wake transition regime of Mode A with large-scale dislocations. For all of the cases with $L_z > 10$, where the simulated λ ranges from 3.50 to 4.33 while $\lambda_A = 3.865$, the quantitative results of the E_z and hydrodynamic forces (Fig. 9 and Fig. 10) do not appear to correlate with the relationship between λ and λ_A. This is likely because after the onset of dislocations, vortex structures are affected by multiple

instability mechanisms such as the ones responsible for both Mode A and Mode B (Williamson, 1996; Thompson et al., 2001) and are no longer largely controlled by the instability mechanism responsible for the intrinsic wavelength of λ_A.

For the relatively ordered Mode B structure at Re = 270, two cases with L_z = 10.6 and L_z = 12.0 are examined. At Re = 270, the linear stability analysis by Posdziech and Grundmann (2001) predicted the most unstable wavelengths for the two modes of λ_A = 3.53 and λ_B = 0.825. Based on the stability analysis results by Posdziech and Grundmann (2001), L_z = 12.0 corresponds to $3.40\lambda_A$ or $14.55\lambda_B$, while L_z = 10.6 corresponds to $3.00\lambda_A$ or $12.85\lambda_B$. The span length of 10.6 with respect to 12.0 is much closer to an integer multiple of λ_A or λ_B. However, the quantitative results obtained from the fully developed flow (t^* = 800 – 1600) for the two cases are extremely close (see Table 2), and the sharp-peaked frequency spectra of C_L are also in close agreement (Fig. 12). This suggests that there is no need to consider the most unstable wavelengths in simulations for this regime with L_z > 10. For both cases, the dominant wake structure is the ordered Mode B, while scattered Mode A (without dislocation) may sometimes be observed along the span as well (e.g. Fig. 13(b)). In Fig. 13(a), the cylinder span width is occupied by 13 pairs of ordered Mode B structure. However, after dividing the cylinder span evenly into 13×2 sections, it is seen that the Mode B vortex pairs are not exactly evenly distributed along the span width, i.e. each pair may have a wavelength λ that is slightly different from λ_B. In addition, with the intermittent appearance of Mode A at random spanwise locations, the simulated λ for the two modes are unlikely influenced by L_z.

Table 2. Quantitative results for the two cases at Re = 270 with different L_z. The variations of the results are represented by the relative differences with respect to the second column.

Quantity	L_z = 10.6		L_z = 12.0	
	Full data length	Second half	Full data length	Second half
St	0.20563	+0.03%	+0.02%	+0.05%
$-C_{pb}$	1.10684	-0.64%	+0.40%	+0.96%
$\overline{C_D}$	1.34865	+0.14%	+0.24%	+0.25%
C_L'	0.56093	+0.77%	+1.25%	+1.29%

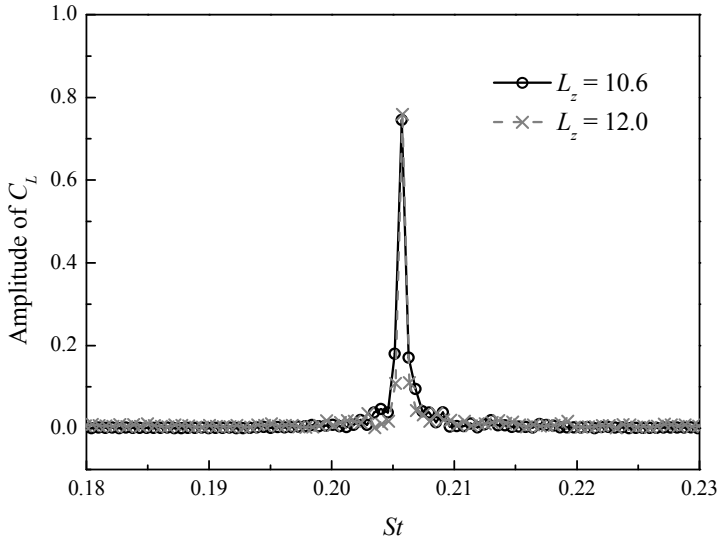

Fig. 12. Frequency spectra of C_L for the two cases at Re = 270 with different L_z.

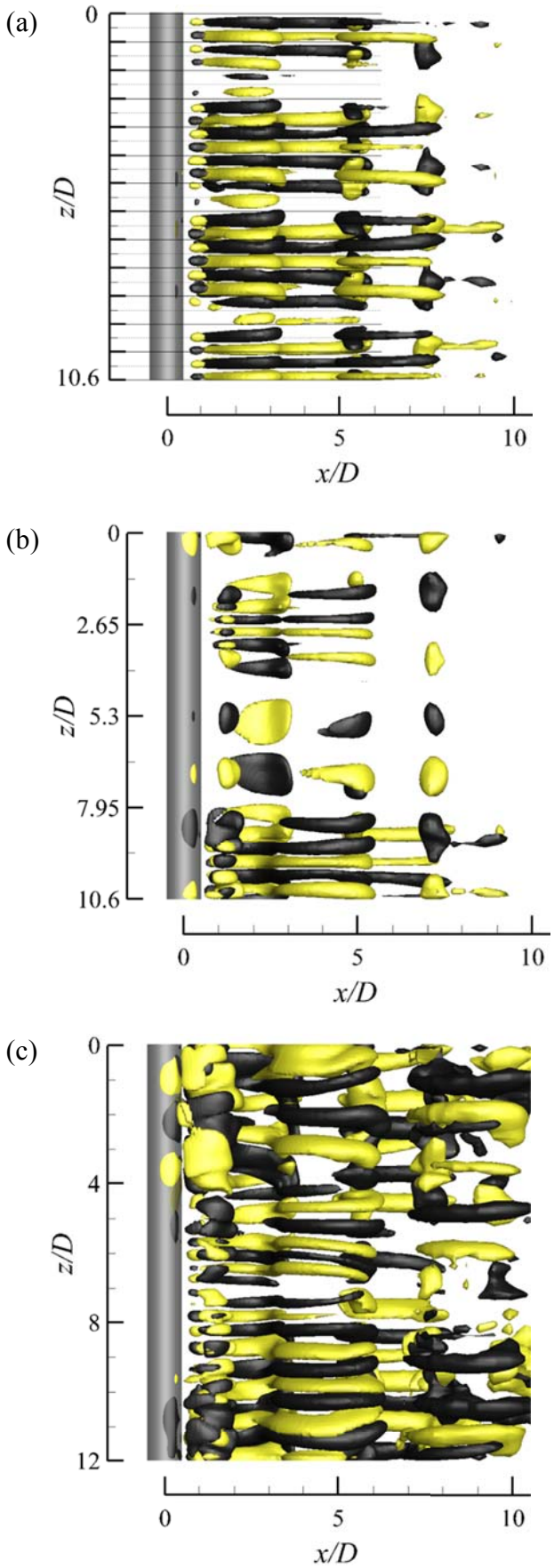

Fig. 13. Iso-surfaces of $\omega_x = \pm 0.5$: (a) case P10.6 at $Re = 270$ and $t^* = 1060$, (b) case

P10.6 at Re = 270 and t^* = 1500, and (c) case P12 at Re = 280 and t^* = 2240. Dark grey and light yellow denote positive and negative values, respectively. The flow is from the left to the right past the cylinder on the left.

It has been demonstrated that for L_z > 10, both Mode A with large-scale dislocations and relatively ordered Mode B are not strongly correlated with the exact wavelengths of λ_A and λ_B, and the simulation results are not strongly dependent on the simulated λ with respect to λ_A and λ_B. It is believed that the above conclusion is also valid for the gradual mode swapping process from Mode A with dislocations to Mode B. The conclusion is also expected to be applicable for Re above 270, as the Mode B structure becomes increasingly disordered, and the wavelength of Mode B becomes increasingly varied along the span width (e.g. Fig. 13(c)). This suggests that for the simulations of the wake transitions above Re_{cr}, the L_z value does not have to be an integer multiple of the most unstable wavelength of Mode A or Mode B.

6. Conclusions

The effects of the spanwise domain length (L_z) and the boundary condition (BC) at the two lateral boundaries perpendicular to the cylinder span on three-dimensional (3D) direct numerical simulation (DNS) results of flow past a circular cylinder are examined. It is found that an over-prediction of the onset point of the secondary wake instability (Re_{cr}) may be attributed to the discrepancy between the simulated wavelength (λ) and the most unstable spanwise wavelength of Mode A (λ_A), rather than an L_z that is not sufficiently long. For the purpose of minimizing the computational cost while maintaining the accuracy of the prediction of Re_{cr}, the use of the symmetry BC and $L_z = \lambda_A/2$ (if λ_A is known *a priori*) is recommended. If λ_A is not known *a priori*, a resolution of 3 pairs of Mode A under the symmetry BC generally indicates a relative error of less than 1% in the prediction of Re_{cr}. The maximum relative error one can expect by using the symmetry BC is less than a half of that from using the periodic BC at the same L_z value.

The predicted vortex structures and hydrodynamic forces in the first 3D wake transition regime of Mode A with vortex dislocations is studied at Re = 200 with both lateral BCs. For L_z within the limit of ~ $1.1\lambda_A$, due to the confinement of L_z to the intrinsic wavelength λ_A, sustained Mode A vortex structure is observed while vortex dislocation is completely suppressed. For $1.1\lambda_A < L_z \leq 9$, although vortex dislocations can be observed, the vortices distributed along the span width are still strongly affected by the insufficiency of L_z. For both lateral BCs, randomly distributed dislocations and converged hydrodynamic forces can only be achieved with $L_z > 10$ (~ $3\lambda_A$). However, when the symmetry BC is applied, the streamwise and transverse vorticities are both forced to be zero at the two lateral boundaries. This restricts the development of the flow three-dimensionality and vorticity for at least $0.5D$ from each end of the span. The periodic BC is free from this restriction.

For the wake transition regimes above Re_{cr}, including Mode A with vortex dislocations, the mode swapping process, and the relatively ordered and disordered Mode B structures, the simulation results with $L_z > 10$ are not strongly dependent on the simulated λ (based on the lateral BC and L_z) with respect to λ_A and λ_B. This is because the dislocations and Mode B structures are not strongly correlated with the exact wavelengths of λ_A and λ_B, and the simulated wavelengths are not strongly influenced by L_z. This suggests that for the simulations of the wake transitions above Re_{cr}, the L_z value does not have to be an integer multiple of λ_A or λ_B.

Acknowledgments

This work was supported by resources provided by the Pawsey Supercomputing Centre with funding from the Australian Government and the Government of Western Australia. The first author would like to acknowledge the support from the Australian Government and the University of Western Australia by providing IPRS and APA scholarships for a doctoral degree, as well as the Australia-China Natural Gas Technology Postgraduate Research Scholarships from the Australian and Western Australian Governments, the North West Shelf Joint Venture Partners, and the Western

Australian Energy Research Alliance. The third author would like to acknowledge the support from the Australian Research Council through Discovery Early Career Research Award (DE150100428).

References

Barkley, D., Henderson, R.D., 1996. Three-dimensional Floquet stability analysis of the wake of a circular cylinder. Journal of Fluid Mechanics 322, 215–241.

Barkley, D., Gomes, M.G.M., Henderson, R.D., 2002. Three-dimensional instability in flow over a backward-facing step. Journal of Fluid Mechanics 473, 167–190.

Behara, S., Mittal, S., 2010. Wake transition in flow past a circular cylinder. Physics of Fluids 22, 114104.

Braza, M., Faghani, D., Persillon, H., 2001. Successive stages and the role of natural vortex dislocations in three-dimensional wake transition. Journal of Fluid Mechanics 439, 1–41.

Carmo, B.S., Sherwin, S.J., Bearman, P.W., Willden, R.H.J., 2008. Wake transition in the flow around two circular cylinders in staggered arrangements. Journal of Fluid Mechanics 597, 1–29.

Gioria, R.S., Meneghini, J.R., Aranha, J.A.P., Barbeiro, I.C., Carmo, B.S., 2011. Effect of the domain spanwise periodic length on the flow around a circular cylinder. Journal of Fluids and Structures 27, 792–797.

Griffith, M.D., Thompson, M.C., Leweke, T., Hourigan, K., Anderson, W.P., 2007. Wake behaviour and instability of flow through a partially blocked channel. Journal of Fluid Mechanics 582, 319–340.

Henderson, R.D., 1997. Nonlinear dynamics and pattern formation in turbulent wake transition. Journal of Fluid Mechanics 352, 65–112.

Issa, R.I., 1986. Solution of implicitly discretized fluid flow equations by operator-splitting. Journal of Computational Physics 62, 40–65.

Jiang, H., Cheng, L., Draper, S., An, H., Tong, F., 2016. Three-dimensional direct numerical simulation of wake transitions of a circular cylinder. Journal of Fluid Mechanics 801, 353–391.

Karniadakis, G.E., Triantafyllou, G.S., 1992. Three-dimensional dynamics and transition to turbulence in the wake of bluff objects. Journal of Fluid Mechanics 238, 1–30.

Labbé, D.F.L., Wilson, P.A., 2007. A numerical investigation of the effects of the spanwise length on the 3-D wake of a circular cylinder. Journal of Fluids and Structures 23, 1168–1188.

Lei, C., Cheng, L., Kavanagh, K., 2001. Spanwise length effects on three-dimensional modelling of flow over a circular cylinder. Computer Methods in Applied Mechanics and Engineering 190, 2909–2923.

Leontini, J.S., Lo Jacono, D., Thompson, M.C., 2015. Stability analysis of the elliptic cylinder wake. Journal of Fluid Mechanics 763, 302–321.

OpenFOAM. Available from www.openfoam.org.

Persillon, H., Braza, M., 1998. Physical analysis of the transition to turbulence in the wake of a circular cylinder by three-dimensional Navier–Stokes simulation. Journal of Fluid Mechanics 365, 23–88.

Posdziech, O., Grundmann, R., 2001. Numerical simulation of the flow around an infinitely long circular cylinder in the transition regime. Theoretical and Computational Fluid Dynamics 15, 121–141.

Rao, A., Thompson, M.C., Leweke, T., Hourigan, K., 2013. The flow past a circular cylinder translating at different heights above a wall. Journal of Fluids and Structures 41, 9–21.

Rao, A., Thompson, M.C., Leweke, T., Hourigan, K., 2015. Flow past a rotating cylinder translating at different gap heights along a wall. Journal of Fluids and Structures 57, 314–330.

Robichaux, J., Balachandar, S., Vanka, S.P., 1999. Three-dimensional Floquet instability of the wake of square cylinder. Physics of Fluids 11, 560–578.

Sheard, G.J., Thompson, M.C., Hourigan, K., 2003. From spheres to circular cylinders: the stability and flow structures of bluff ring wakes. Journal of Fluid Mechanics 492, 147–180.

Thompson, M.C., Leweke, T., Williamson, C.H.K., 2001. The physical mechanism of transition in bluff body wakes. Journal of Fluids and Structures 15, 607–616.

Tong, F., Cheng, L., Zhao, M., Zhou, T., Chen, X., 2014. The vortex shedding around four circular cylinders in an in-line square configuration. Physics of Fluids 26, 024112.

Williamson, C.H.K., 1992. The natural and forced formation of spot-like ‘vortex dislocations’ in

the transition of a wake. Journal of Fluid Mechanics 243, 393–441.

Williamson, C.H.K., 1996. Three-dimensional wake transition. Journal of Fluid Mechanics 328, 345–407.

Zhao, M., Thapa, J., Cheng, L., Zhou, T., 2013. Three-dimensional transition of vortex shedding flow around a circular cylinder at right and oblique attacks. Physics of Fluids 25, 014105.